arXiv:1111.6012v1 [cond-mat.mtrl-sci] 25 Nov 2011

Polariton states bound to defects in GaAs/AlAs planar microcavities

Joanna M Zajac* and Wolfgang Langbein
School of Physics and Astronomy, Cardiff University, The Parade, Cardiff CF24 3AA, United Kingdom

Maxime Hugues and Mark Hopkinson
Department of Electronic and Electrical Engineering, University of Sheffield. Mappin Street, Sheffield S1 4JD, UK

(Dated: November 28, 2011)

We report on polariton states bound to defects in planar GaAs/AlAs microcavities grown by molecular beam epitaxy. The defect types relevant for the spatial polariton dynamics in these structures are cross-hatch misfit dislocations, and point-like defects extended over several micrometers. We attribute the latter defects to Ga droplets emitted occasionally by the Ga cell during the growth. These defects, also known as oval defects, result in a dome-like local modulation of surface, which is translated into the cavity structure and leads to a lateral modulation of the cavity polariton energy of up to 15 meV. The resulting spatially localized potential landscape for the in-plane polariton motion creates a series of bound states. These states were characterized by spectrally resolved transmission imaging in real and reciprocal space, and reveal the spatial potential created by the defects. Interestingly, the defect states exhibit long lifetimes in the 10 ps range, which we attribute to a spatially smooth confinement potential.

I. INTRODUCTION

Semiconductor microcavities have been extensively studied in last 20 years[1–3]. Significant attention was given to planar microcavities, which are Fabry-Perot resonators, with a photon mode confined in growth direction by Bragg mirrors made of pairs of $\lambda/4$ layers of alternating refractive index. The in-plane dispersion of the mode is close to quadratic for in-plane wavevectors k much smaller than the free-space wavevector, with a curvature described by an effective mass about 4 orders of magnitude smaller than the free electron mass. This implies a significant dispersion within the external optically accessible wavevector range. When coupled to a quantum well exciton, these microcavities allow to investigate fundamental condensed-matter phenomena like strong coupling, Bose-Einstein condensation, lasing, parametric amplification, etc. In many cases, these effects are significantly affected by the disorder in the structures. This leads to localization of the Bose-Einstein condensate, formation of vortices and can be used as a probe for the dynamics and excitations the polaritonic superfluid phase[4–6].

The spatial localization of the cavity mode by artificial in-plane structures was investigated experimentally and theoretically in Refs. 7–11. In these works, circular mesas with diameters of 3-19 μm and heights in the nanometer range were created by lithography on the cavity layer before growing the top Bragg mirror.

In nominally planar samples it is typically observed that the cavity mode is elastically scattered on a cross-hatched dislocation pattern[12–16], while the excitonic part tends to exhibit a more isotropic disorder on the relevant micrometer length scale. In samples grown by MOCVD, additional random disorder is observed, indicating a fluctuation of the layer thickness in the micrometer spatial range due to the growth mode influenced by transport of the reactants via the gas-phase, allowing for non-homogeneous deposition. In MBE instead, the molecular beam guarantees the random deposition of Ga atoms, and the surface diffusion, which is limited to typically 100 nm, cannot create a long-range thickness modulation.

Apart from the cross-hatch dislocation pattern, one typically observes point-like defects (PD) with a surface density of about $10^4/\mathrm{cm}^2$, which have a size and shape typical of those ascribed as oval defects[17]. PDs are better visible in the regions of lower density of cross-hatches, however were observed in all regions, and for different MC samples which we investigated until now. They are not related to strain relaxation, but are generally attributed to particle contamination during growth or Ga source spitting[18]. These defects produce rather extended surface modulations, typically without lattice defects. Polariton modes in MCs have typical extensions of 10-100 micrometers, limited by mirror transmission or residual disorder. These modes are therefore sensitive to the length-scale of the PDs, making an excellent probe for structure inhomogeneities in the 1-100 micrometer range. The resonant local transmission of the MC is modified by the PDs, creating spatially confined cavity modes, typically visible as a series of spectrally narrow localized modes, as will be shown here. The paper is organized as follows. In Section II the details of the samples and the experiment are given, followed by a description of the disorder inside these structures in Section III, and a presentation of the results of the optical measurements on localized states in Section IV. The origin of PDs is discussed in Section V.

II. SAMPLE AND EXPERIMENT

The sample investigated in this work is a bulk $1\,\lambda_c$ GaAs semiconductor microcavity (MC) surrounded by AlAs/GaAs distributed Bragg reflectors (DBRs) with 27 (24) $\lambda_c/4$ pairs on the bottom (top), respectively. Images of a sample are shown on Fig. 1. At a temperature of T=80 K, the cavity mode energy was $E_C = 1.485$ eV,

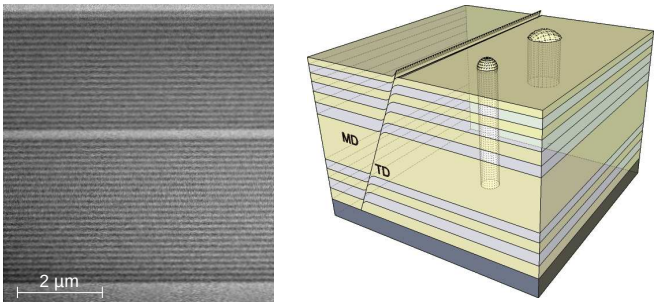


FIG. 1: Scanning electron micrograph of the studied microcavity (left), and sketch of the sample structure (right) showing examples of defects, starting from different layers across the structure.

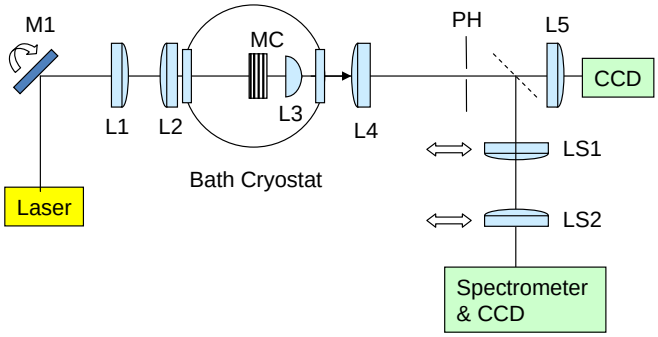


FIG. 2: Sketch of the optical setup used to measure the localized polariton states. Both real-space and reciprocal space imaging was used. L1-L5 Lenses, MC: Microcavity sample LS1,LS2 moving lenses for imaging, for details see text.

red detuned by 23 meV from the bulk GaAs exciton in the cavity layer at 1.508 eV. The structure was grown under continuous wafer rotation, resulting in a very weak (<1%) thickness variation from the center to the edge of the wafer.

The optical measurements of the polariton states were conducted at nitrogen temperature (T=80 K) with the sample mounted strain-free in a bath cryostat. Real and reciprocal space transmission spectra were taken in the low-intensity regime. A sketch of the setup is shown on Fig. 2.

Two different optical excitation configurations were used. Firstly, a single-mode external cavity diode laser (Sacher Lynx) with 5 MHz linewidth was employed to excite the polaritons at normal incidence ($\mathbf{k} = 0$) over a large size in real space ($\sim$ 1 mm) from the substrate side. This excitation allowed to selectively image a specific polariton energy with a spectrally integrating detector. Secondly, a mode-locked Ti:Sapphire laser (Coherent Mira) was used providing 100 fs pulses at 76 MHz repetition rate. The large spectral width of approximately 20 meV allows to excite polariton bound states and the continuum dispersion simultaneously. The excitation was spatially focussed to a spot of about 3 μm diameter using a lens of 0.15 numerical aperture, corresponding to an excitation wavevector range of $|\mathbf{k}| < 1.1/\mu$m. The emission was collected from the epi-side by an aspheric lens of 0.5 NA (L3 in Fig. 2) with a wavevector range of $|\mathbf{k}| < 4/\mu$m, providing a spatial resolution of about 1 μm. The emission was detected spectrally integrated in the real or reciprocal space using video CCD cameras. For spectrally resolved detection, the emission was imaged in real or reciprocal space into the input slit of an imaging spectrometer with 12 μeV spectral resolution. Two-dimensional images were acquired by translating the image across the spectrometer slit using lateral movements of two lenses (LS1 and LS2 in Fig. 2). Scans were made with 0.5 μm (real space), or 0.05 μm^{-1} (reciprocal space) steps.

III. DISORDER VARIATION VERSUS GROWTH TEMPERATURE

During the growth of the investigated structure, the temperature was ramped up to 715 °C for the AlAs layers, and down to 660°C for the Bragg GaAs layers, and to 630°C for the GaAs cavity layer. For comparison, in Ref. 19 the sample was grown at a constant temperature of 620 − 630°C. A radial non-uniformity of the back-surface roughness due to As evaporation and resulting Ga-droplet formation was observed (see Fig. 3g). This indicates that the growth temperature was non-uniform across the wafer, an effect which is significant due to the usage of an undoped and back-side polished 3-inch wafer, leading to a weaker radiative coupling to the surrounding compared to doped wafers, increasing the infrared absorption, and unpolished wafers, decreasing the reflection and avoiding radiation trapping by total-internal reflection. The cavity resonance energy was varying by only 0.5 % over the wafer, indicating an exceptional flux homogeneity of the Ga and Al cells. The polariton disorder instead was found to vary significantly as function of radial position R on the wafer, as shown in Fig. 3a)-f) where transmission images and spectra are shown at different R. Close to the center ($R = 4$ mm), a cross-hatch pattern is visible and the polariton states excited at $k = 0$ show an inhomogeneous broadening of $\sim 100\,\mu$eV. This cross-hatch disorder decreases with increasing radius, and is not discernible at $R = 32$ mm close to the edge of the wafer. The cross-hatch pattern is due to the formation of a misfit-dislocation pattern found in (001) oriented strained cubic semiconductor thin film systems[20]. It is formed by strain relaxation via slides along the {111} slip planes, which form lines along [110] and [1$\bar{1}$0] at their intersection with the film surface. Such a pattern is only observed for weakly strained films ($\epsilon < 2\%$), while for higher strains Stranski-Krastanov or Volmer-Weber growth is found. Cross-hatch patterns are typically reported for a lattice mismatch of the order of 1%, leading to a large density of slip lines and a significant surface modulation of several nanometers. The lattice mismatch of the GaAs/AlAs Bragg mirrors at room temperature[21] is 0.14%. Using a mismatch of 0.07% of a Bragg period, we find a critical thickness for strain relaxation[22]

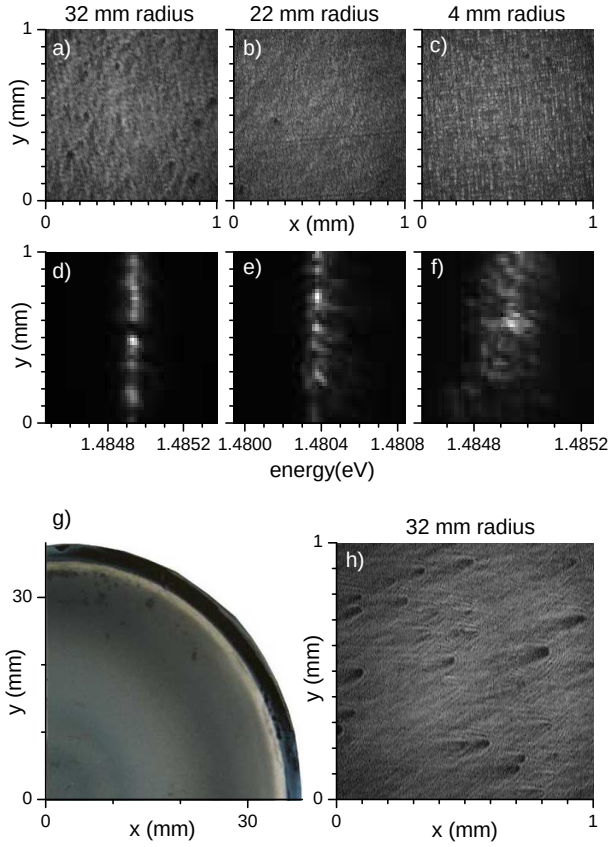


FIG. 3: Disorder variation across the 3 inch wafer. Transmitted intensity for excitation at $\mathbf{k} = 0$ with 100 fs pulses resonant to the cavity mode for samples from different radial positions on the wafer as indicated. a),b),c) spatially resolved, spectrally integrated. d),e),f) spectrally resolved as function of y at a given x position. Linear gray scale from zero (black) to white. g) Image of the back side of the wafer. h) as a), but for excitation at $\mathbf{k} \approx (-0.3, 0)/\mu$m.

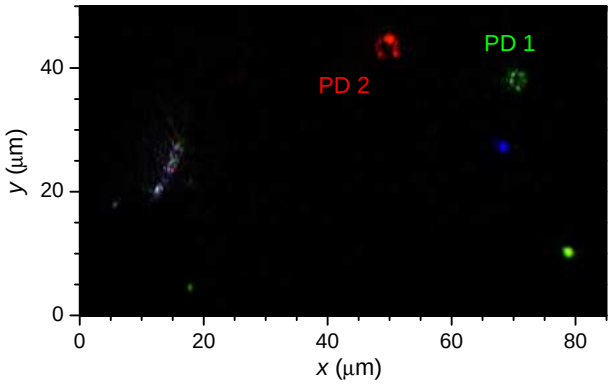


FIG. 4: Spatially resolved color coded transmission intensity for photon energies of 1482.1 meV (blue channel), 1482 meV (magenta channel), and 1473.8 meV (yellow channel), see movie in supplementary materials where relevant energy tuning range is 1482.1 - 1473.8 eV. Two localized states are labeled PD 1 and PD 2 for later reference.

of about 2 μm. The Bragg mirrors have a total thickness of 6 μm, exceeding the critical thickness, and misfit dislocations form. However, the mismatch decreases with temperature[21,23], providing a lattice matched system at about 900 °C. We can therefore expect that the growth temperature influences the cross-hatch formation.

In the wafer region with low cross-hatch disorder ($R =$ 32 mm) the polariton linewidths are within 30 μeV over extended regions. This exceptional spatial homogeneity is confirmed by the propagation of polaritons over hundreds of micrometers visible in Fig. 3 h), where the interference pattern of freely propagating polaritons with the ones scattered by the PDs is observed for oblique excitation a few degrees from normal corresponding to $\mathbf{k} \approx (-0.3, 0)/\mu$m. PDs are visible in all sample regions, and form natural defects which we investigate further in the subsequent sections.

IV. POLARITON STATES BOUND TO POINT-LIKE DEFECTS

The spatial distribution of polariton energies can be visualized by resonant excitation with a spectrally narrow source. We used a single-mode external cavity diode laser (Sacher Lynx) with 5 MHz linewidth to excite the polaritons at normal incidence ($\mathbf{k} = 0$) over a large size in real space ($\sim$ 1 mm) from the substrate side. The emission from the epi side was imaged onto a CCD. By tuning the excitation photon energy below the band edge of the extended cavity polaritons, individual localized states can be excited resonantly and appear as bright spots. By scanning the photon energy, the localized defect states within the excited area are sequentially addressed according to their eigenenergy.

An example is shown in Fig. 4, where images corresponding to three different excitation photon energies are overlayed into a color image. The different colors of the localized states show their different eigenenergies $\hbar\omega_n$. Different shapes of the localized states are also visible, and we find an average distance of a few 10 μm of the PDs with localized states separated by more than 1 meV from the band edge. To gain more detailed information about the set of states bound to an individual PD, we change excitation and detection setup to the pulsed 100 fs source centred $\sim$ 10 meV below the polariton band-edge, spatially focussed onto the PD. The emission was measured using spectrally resolved imaging in either real or reciprocal space, as discussed in section II.

The resulting data for the polariton states bound to PD 1 are shown in Fig. 5. On the left the directionally and spectrally resolved intensity $I(k_x = 0, k_y, \omega)$ is given on a logarithmic scale showing bound resonances and the continuum. A series of $n_1 = 15$ discrete resonances is discernable, at frequencies ω_n, $n = 1..n_1$. The intensity distributions at these resonances in real and reciprocal space, $I(x, y, \omega_n)$ and $I(k_x, k_y, \omega_n)$, respectively, are proportional to the probability distributions $|\Psi_n|^2$ of the corresponding state wavefunctions Ψ_n (assuming that the Bragg mirror reflectivity is independent of $\mathbf{k}$ and all relevant emission directions $\mathbf{k}$ are imaged). For convenience we show the localization energy $\Delta_n = \hbar\omega_n - \hbar\omega_c$ of the states, where $\hbar\omega_c$ is the band edge given by the minimum of the parabolic dispersion of the free polaritons.

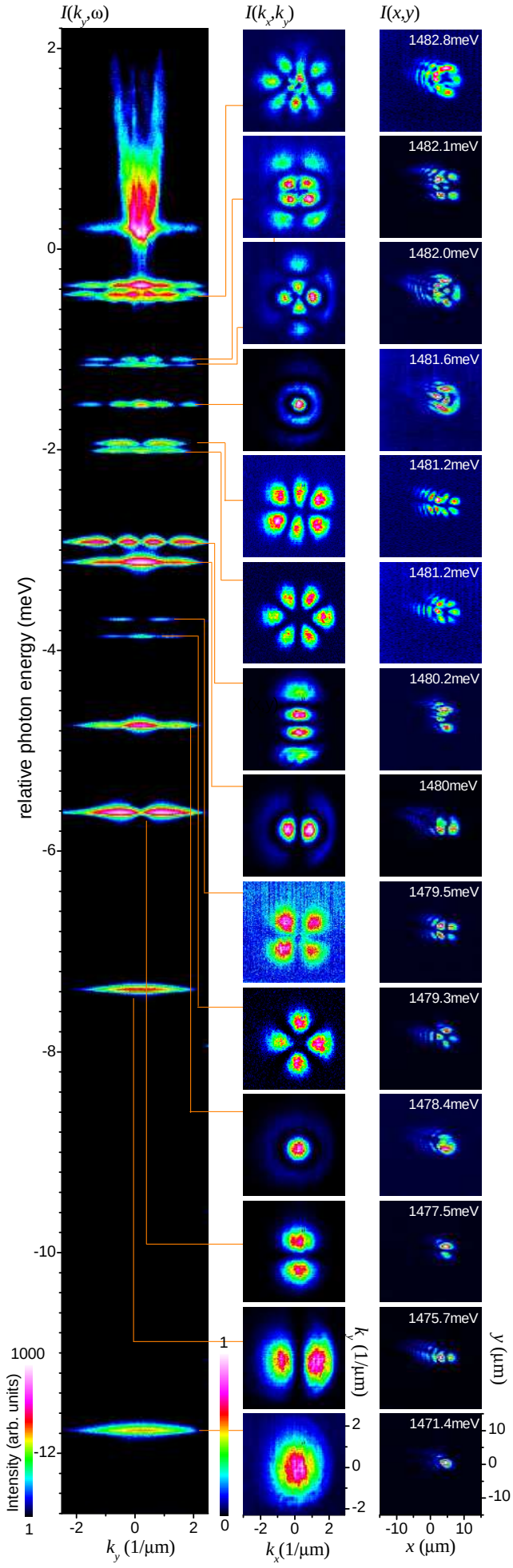


FIG. 5: Spectral imaging of the emission from polariton states close to PD 1 of Fig. 4 in real and reciprocal space. Left: intensity $I(k_x = 0, k_y, \omega)$ on a logarithmic color scale as indicated. The energy $\hbar\omega$ is shown relative to the polariton band edge at $\hbar\omega_c = 1.4833\,\text{eV}$. The intensity of the individual states is given in reciprocal space $I(k_x, k_y, \omega_n)$ in the middle column and in real space $I(x, y, \omega_n)$ in the right column. They are shown using a linear color scale and are individually normalized to their maximum. The resonance energies $\hbar\omega_n$ are given, and the connection lines indicate the corresponding state in $I(k_x = 0, k_y, \omega)$. The tails visible in $I(x, y, \omega_n)$ are due to imaging abberations relevant at large $\mathbf{k}$.

The ground state Ψ_1 is observed at $\Delta_1 = -11.9\,\text{meV}$. Some resonances are observed even above the continuum, indicating the presence of a potential barrier between the defect region and the surrounding continuum. These states could lead to resonant scattering similar to Feshbach resonances observed in atomic physics. The shapes of the wavefunctions reveal a nearly cylindrical symmetry of the effective confinement potential $V_1(x, y)$ created by PD 1. The first excited state Ψ_2 is found at $\Delta_2 = -7.6\,\text{meV}$, and shows a p_x-like symmetry, with a node at $x = 0$. Ψ_3 has $\Delta_3 = -5.8\,\text{meV}$ and a p_y-like symmetry with a node at $y = 0$. The energy splitting of $\Psi_{2,3}$ shows a breaking of cylindrical symmetry of $V_1(x, y)$. The next 3 states correspond to d-states, Ψ_4 having zero angular momentum and 2 nodes in radial direction, and $\Psi_{5,6}$ being superpositions of angular momentum 2. The non-degeneracy of the different n=2 states shows the non-parabolicity of the confinement. The higher states can be classified in a similar way with increasing number of nodes in the wavefunction.

PD 2 instead is not cylindrically symmetric as shown in Fig. 6. The two lowest states $\Psi_{1,2}$ are separately localized to the left and the right of the defect center with a s-like wavefunction, indicating two separate minima of the potential. The left minimum confines also a p-like excited state Ψ_3, while the corresponding excited state on the right Ψ_4 is already extended along a horseshoe-shaped region, coupling to a d-like state of the left minimum. The next state Ψ_5 is a mixture of the left f-like state with the right d-like state. Ψ_6 is mostly localized on the tip of the horseshoe, possibly due to a local potential maximum close to the state energy, which is supported by the relatively small wavevector spread in k_x. A total of $n_3 = 11$ states are visible.

The last reported defect, PD 3 (see in Fig. 7, not shown in Fig. 4) is similar to PD 1 in being approximately circular symmetric, but about a factor of 3 shallower. The ground state Ψ_1 is s-like, and shows a larger extension in real space and a smaller in reciprocal space than the ground state of PD1, as expected from the weaker confinement. A total of $n_3 = 12$ states are visible.

A. Coherent wavepacket dynamics

The two p-like excited states $\Psi_{2,3}$ of PD 3 are nearly degenerate ($\approx 100\,\mu\text{eV}$ separation). Due to the co-

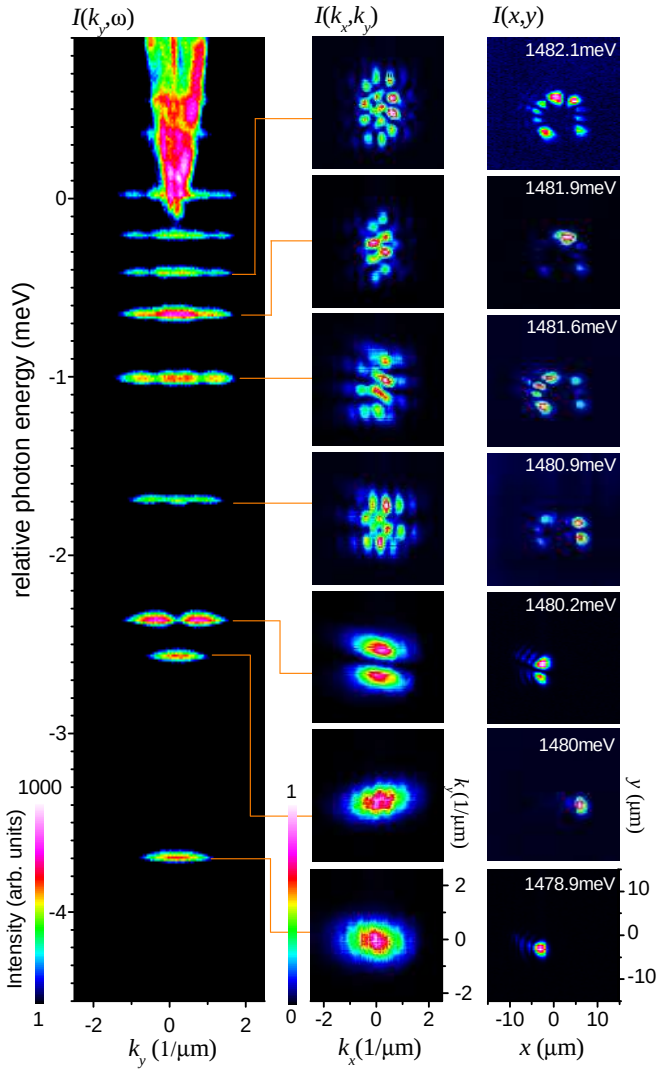


FIG. 6: As figure 5, but for PD 2 of Fig. 4 and $\hbar\omega_c = 1.4826$ eV.

herent excitation of the states and their finite spectral width, the emitted field is a coherent superposition of the two wavefunctions $a\Psi_2 + b\Psi_3$, with amplitudes determined by the excitation. To compare the measurements with the theoretically expected result, we assume harmonic confinement and p-like wavefunctions $\Psi_{2,3} \propto (k_x, k_y) \exp\left(-\frac{k_x^2+k_y^2}{a^2}\right)$ with frequencies $\omega_{2,3} = \omega_0 \pm \Delta_\mathrm{p}$ and linewidths γ_p which are a sum of the state linewidth and spectrometer resolution. The measured wave-function can be modeled as a coherent superposition of the two near-resonant states with a relative phase ϕ and amplitude η given by the excitation conditions. This superposition can be written as

$$\Psi(\omega) \propto \left(\frac{k_x}{\omega - (\omega_0 - \Delta_\mathrm{p}) + i\gamma_\mathrm{p}} + \eta e^{i\phi} \frac{k_y}{\omega - (\omega_0 + \Delta_\mathrm{p}) + i\gamma_\mathrm{p}}\right) e^{-\frac{k_x^2+k_y^2}{a^2}} \quad (1)$$

Similarly, for the d-like $l = 2$ states $\Psi_{5,6} = (k_x k_y, k_x^2 - k_y^2) \exp\left(-\frac{k_x^2+k_y^2}{a^2}\right)$ with frequencies $\omega_{5,6} = \omega_0 \pm \Delta_d$ and linewidth γ_d,

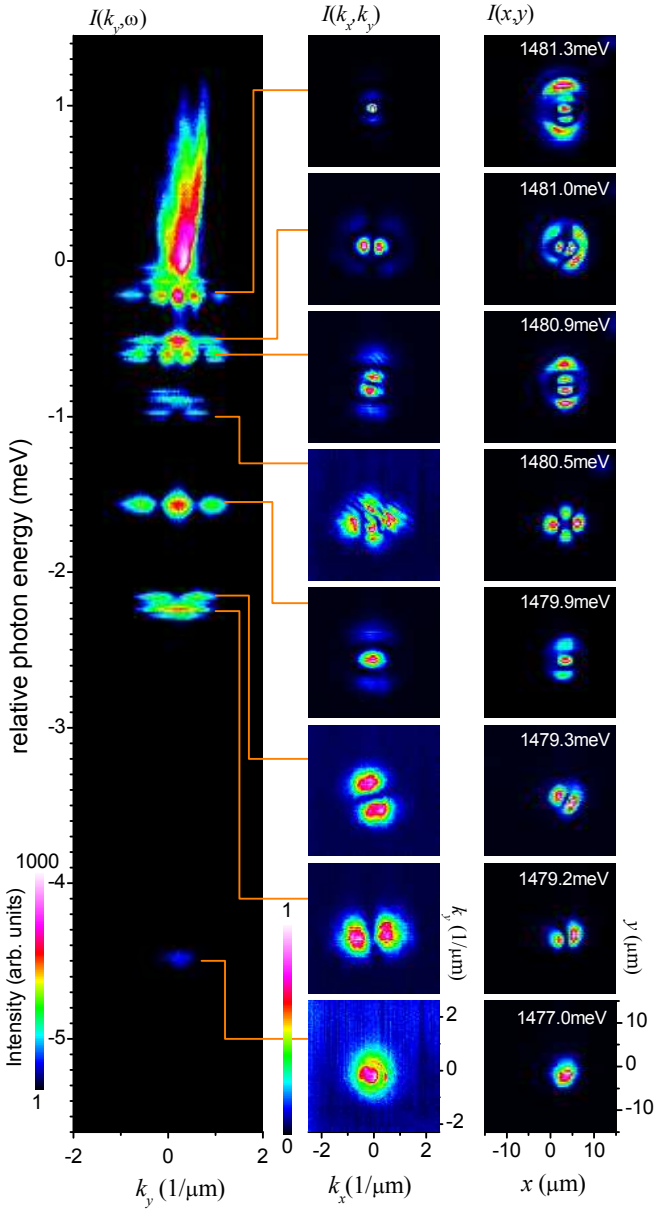


FIG. 7: As figure 5 but for PD 3, (not shown on Fig. 4), and $\hbar\omega_c = 1.4815$ eV.

$$\Psi(\omega) \propto \left(\frac{k_x k_y}{\omega - (\omega_0 - \Delta_\mathrm{d}) + i\gamma_\mathrm{d}} + \eta e^{i\phi} \frac{k_x^2 - k_y^2}{\omega - (\omega_0 + \Delta_\mathrm{d}) + i\gamma_\mathrm{d}}\right) e^{-\frac{k_x^2+k_y^2}{a^2}} \quad (2)$$

Simulations were done using parameters values as indicated in Fig. 8, and give a qualitative agreement with measurements. A movie over the detuning is available in the online material.

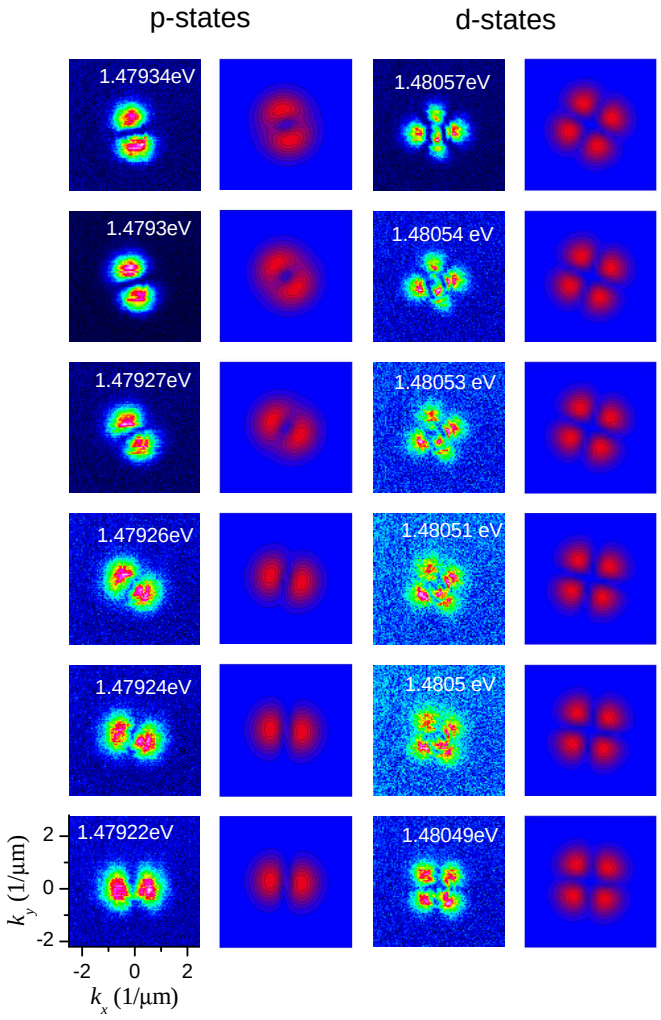


FIG. 8: Measured intensities $I(\mathbf{k},\omega)$ (left columns) and simulated $|\Psi(\omega)|^2$ for energies close to the p-states (left) and d-states (right). The energy is increasing from lower to upper panels as labeled. The parameters used were $\hbar\omega_0 = 1.479205\,\mathrm{eV}$, $\hbar\Delta = 90\,\mu\mathrm{eV}$, $\hbar\gamma_1 = 58\,\mu\mathrm{eV}$, $\hbar\gamma_2 = 73\,\mu\mathrm{eV}$, $\eta = 1$, $\phi = 0$ for the p-states, and $\hbar\omega_0 = 1.48047\,\mathrm{eV}$, $\hbar\Delta = 89\,\mu\mathrm{eV}$, $\hbar\gamma_1 = 37\,\mu\mathrm{eV}$, $\hbar\gamma_2 = 50\,\mu\mathrm{eV}$,$\eta = 1$, $\phi = 0$ for the d-state simulation.

B. Confining potential

The observed localized polariton states can related to an effective confinement potential $V_m(\mathbf{r})$ for the in-plane polariton motion. We can estimate $V_m(\mathbf{r})$ using the spectrally integrated density of states $D_m(\mathbf{r})$ created by $V_m(\mathbf{r})$ below the continuum edge in the following way. On the one hand, this density can be calculated from the spatially resolved bound density of states

$$D_m(\mathbf{r}) = \sum_{n=1}^{n_\mathrm{m}} |\Psi_n(\mathbf{r})|^2 \qquad (3)$$

where the bound state probability densities $|\Psi_n(\mathbf{r})|^2$ are taken as the normalized measured intensity

$$|\Psi_n(\mathbf{r})|^2 = \frac{I(\mathbf{r},\omega_n)}{\int I(\mathbf{r},\omega_n) d\mathbf{r}^2} \qquad (4)$$

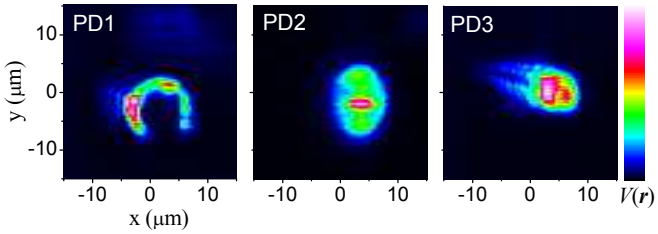


FIG. 9: Confinement potential $V_m(\mathbf{r})$ estimated from the bound density of states $D_m(\mathbf{r})$ for the three PDs, on a color scale as given from 0 (black) to -2.3 meV.

This expression assumes that the emission intensity is proportional to the polariton wavefunction, which is valid for a cavity lifetime which is constant for the in-plane wavevector components of the bound states. This is a reasonable approximation for the data shown here.

On the other hand, $D_m(\mathbf{r})$ is given by the integral of the free density of states from zero kinetic energy at the potential floor to the continuum when neglecting the spatial variation of the confinement potential, *i.e.* in the limit of small level splitting compared to the confinement potential. In two dimensions the density of states is constant and given by $D_{2D} = m/(2\pi\hbar^2)$, such that the integral is simply given by $-V_m(\mathbf{r})D_{2\mathrm{D}}$, and we find $V_m(\mathbf{r}) = -D(\mathbf{r})/D_{2\mathrm{D}}$. We use the effective mass of the polaritons from the measured dispersion $m = 2\cdot10^{-5}\,m_\mathrm{e}$, where m_e is the free electron mass. The resulting confinement potentials for the three investigated PDs are shown in Fig. 9. The symmetry of the potentials reflect the symmetry of the localized states. Comparing with the energies of the confined states, $V_m(\mathbf{r})$ seems generally a factor of 2 to 3 to small. Errors in the scaling of $V_m(\mathbf{r})$ are related to the length calibration of the imaging, which we estimate to have an accuracy of 10%, yielding a 20% error in $V_m(\mathbf{r})$, and to the effective mass m which we estimate to have an error of 10%, resulting in a total of 30% systematic error of the scaling. The finite amount of levels in the potential leads mostly to residual spatial oscillations, while the average potential is reproduced to a relative error of $1/n_\mathrm{m}$, so about 10-20% in our case. A direct comparison of the polariton states in the confining potential $V_m(\mathbf{r})$ could be used to determine the underlying potential in a more quantitative fashion.

V. ORIGIN OF THE POINT-LIKE DEFECTS

The formation of the PDs could be due to a variety of different physical processes. Among them, there are threading dislocations(TD), either propagating from the substrate or created in the epilayers due to surface defects. Usually by growing multilayer structures threading dislocations from the substrate are suppressed as they bend on GaAs/AlAs interfaces and propagate parallel to the ⟨110⟩ directions suppressing the dislocation density even to 5% of its original value[24]. The investigated sample was grown on a wafer with a TD density of about $2\cdot10^3/\,\mathrm{cm}^2$ specified by manufacturer, which is comparable to the observed defect density.

In order to investigate if the observed PD are related to threading dislocations, we used an etching procedure[25,26], which requires less equipment and sample preparation as compared to the alternative method of transmission electron microscopy. It also allows to investigate large surface areas, which is necessary considering the small defect density. Since the sample is not destroyed in the process, it is possible to spatially correlate the etched pits corresponding to the treading dislocations with the PDs. We used the procedure described in Ref. 25 for GaAs etching of {100} crystal facets. The sample was kept in KOH etch at 360 °C for 2 minutes. The resulting etch-pits on the sample surface were observed in a reflective DIC (Differential interference contrast) optical microscope. We found an etch-pit density of about $10^3/\,\mathrm{cm}^2$, consistent with the manufacturer specification. An overview of several defects obtained using DIC microscopy is shown in figure Fig. 10. Each rectangular etch pit marks a threading dislocations in its center. The lines are scratches on the sample surface and/or misfit dislocations.

Subsequently the low temperature transmission measurements were repeated together with reflection microscopy. The positions of the PDs were found to be not correlated to the etch-pits. Instead, the PDs coincide with the round to oval structures of 7-10 micrometer diameter on the sample surface, as observed in Fig. 10. These defects are thus the origin of the localization potentials for the polaritons.

From the DIC images, we have quantitatively extracted the surface profile of the PDs. They show a typical surface height modulation of several tens of nanometers, being approximately parabolic with a small depression about 10% of the height below the original surface at the edge, and a width of a few μm. The energy barrier to the continuum observed in the localized states (see Section IV) is likely to be related to this edge depression.

Also atomic force microscopy images of the surface were obtained, but due to the large extension and small height of the PDs no reliable results of the large scale topology could be extracted.

Using field emission scanning electron microscopy(FESEM), the structures were imaged under grazing angle of incidence (70° to the surface normal) to enhance the contrast for the flat surface topology, and results are shown in Fig. 10. The shape is consistent with the DIC images. A ridge shaped structure close to the center of the dome is also visible.

Growth related defects were categorized in Ref. 18, showing some defects which qualitatively resemble the ones discussed here. We observed defects with different shapes, with the most common being nearly round defects with a weak ridge in the center, as shown on Fig. 10. According to Ref. 18 round defects with nucleus originate from Ga oxide or spitting, while obscure ovals arise from Ga droplets, oxides or particle contaminants. We attribute the observed defects to Ga nano-droplets emitted by the the Ga cell during growth. Once deposited on the surface, the Ga is converted to GaAs, forming a hill with a depression in the center due to the growth kinetics. During the subsequent growth, lateral Ga diffusion leads to an extension of the hill while its height is reduced. Interestingly, we observe nearly round defects in the present sample, while on similar samples grown throughout at a lower temperature of 630°C similar defects are observed, which are elliptical with an about 1:3 ratio of extension in the [110] to [1$\bar{1}$0] directions. We attribute this observation to the temperature-dependent anisotropic Ga mobility on the surface.

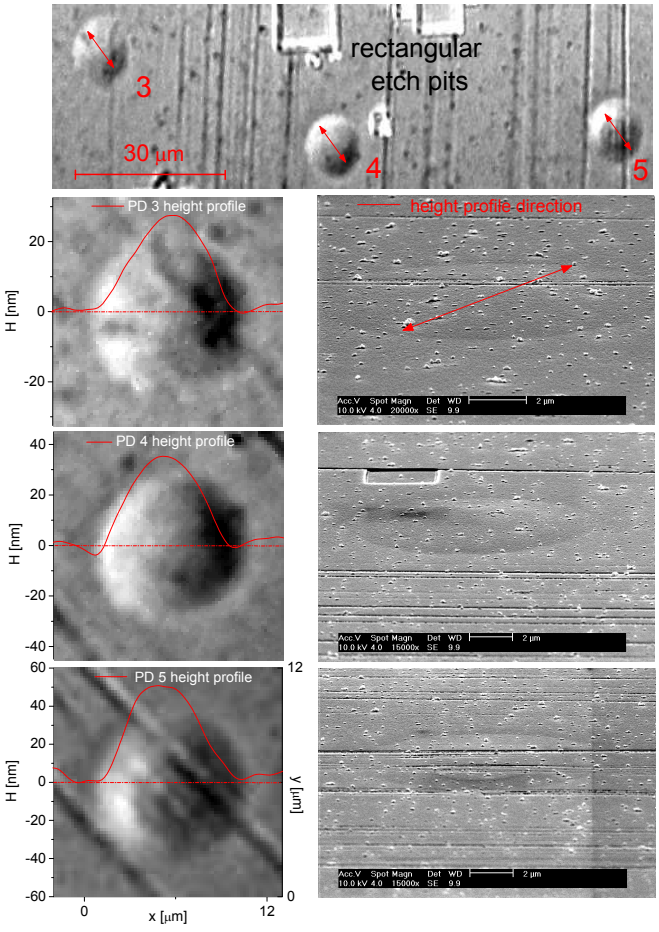


FIG. 10: Top: Sample surface after KOH etching imaged with DIC. Round defects corresponding to PDs are labeled. Below on the left column,individual height profiles of PDs obtained using DIC with the corresponding DIC images. In the right column, corresponding FESEM images of the PDs.

Clearly the impact of such a structure on the polaritons depends on the position of the Ga droplet deposition within the MC structure in growth direction. This information is not accessible in the characterization techniques reported here, which are all measuring the surface topology of the structure. To investigate this further, we used combined focussed ion beam (FIB) - scanning electron beam (SEM) to cut with FIB into the structure and measure the exposed side-wall by SEM[27]. By sequentially slicing the structure, a volume information on the defect is obtained. The results of this investigation including a study on the their influence of the droplet positions relative to the cavity layer on polariton confinement will be reported in a forthcoming work.

VI. SUMMARY

In summary, we have identified point-like defects in planar microcavities which lead to series of spectrally sharp localized polariton states. The localized polariton states were characterized in real and reciprocal space and the underlying confinement potential has been reconstructed from these measurements. The symmetry of the states can be very close to cylindrical. The origin of the defects is attributed to spitting of the Ga cell during MBE growth, depositing Ga droplets of a size of the order of 100 nm onto the sample surface during growth. Due to the large thickness of microcavity structures, the surface density of these droplets is enhanced, and the spatially extended polariton states are exceptionally sensitive to the resulting extended structural variations. The induced confinement potential can be rather smooth, allowing for confined states of small linewidth since the scattering into the lossy microcavity modes at high wavevectors is suppressed.

Acknowledgments

We thank A. Drevisi and I. Fallis for assistance with the KOH etching. This work was supported by the EPSRC UK Research Council (grant n. EP/F027958/1). Author contributions: WL designed the samples, MH and MH grew the samples at the EPSRC National Centre for III-V Technologies, Sheffield, UK, and gave feedback on sample design, JZ performed the structural measurements, JZ and WL performed the optical measurements, analyzed the data and prepared the manuscript.

* Electronic address:ZajacJM@cardiff.ac.uk

[1] A. Kavokin, J. J. Baumberg, G. Malpuech, and F. P. Laussy, *Microcavities* (OUP Oxford, 2007).
[2] A. Q. B. Deveaud-Plédran and P. Schwendimann, eds., *Quantum Coherence in Solid State Systems*, vol. 171 of *International School of Physics Enrico Fermi* (IOS Press, 2009).
[3] M. S. Skolnick, T. A. Fisher, and D. M. Whittaker, Semicond. Sci. Technol. **13**, 645 (1998).
[4] J. Kasprzak, M. Richard, S. Kundermann, A. Baas, P. Jeambrun, J. Keeling, F. Marchetti, M. H. Szymańska, R. André, J. Staehli, et al., Nature **443**, 409 (2006).
[5] K. G. Lagoudakis, M. Wouters, M. Richard, A. Baas, I. Carusotto, R. André, D. L. S. Dang, and B. Deveaud-Pledran, Nature Physics **4**, 706 (2008).
[6] A. Amo, J. Lefrère, S. Pigeon, C. Adrados, C. Ciuti, I. Carusotto, R. Houdré, E. Giacobino, and A. Bramati, Nature Physics **5**, 805 (2009).
[7] R. I. Kaitouni, O. E. Daïf, A. Baas, M. Richard, T. Paraiso, P. Lugan, T. Guillet, F. Morier-Genoud, J. D. Ganière, J. L. Staehli, et al., Phys. Rev. B **74**, 155311 (2006).
[8] P. Lugan, D. Sarchi, and V. Savona, phys. stat. sol. (c) **3**, 2428 (2006).
[9] R. Cerna, D. Sarchi, T. K. Paraïso, G. Nardin, Y. Lèger, M. Richard, B. Pietka, O. E. Daif, F. Morier-Genoud, V. Savona, et al., Phys. Rev. B **80**, 121309(R) (2009).
[10] R. Cerna, T. Paraiso, Y. Leger, M. Wouters, F. Morier-Genoud, M. Portella-Oberli, and B. Deveaud-Plédran, Phys Rev B **81**, 113306 (2010).
[11] G. Nardin, Y. Léger, B. Pietka, F. Morier-Genoud, and B. Deveaud-Plédran, Phys. Rev. B **82**, 045304 (2010).
[12] M. Gurioli, F. Bogani, D. S. Wiersma, P. Roussignol, G. Cassabois, G. Khitrova, and H. Gibbs, Phys. Rev. B **64**, 165309 (2001).
[13] W. Langbein and J. M. Hvam, Phys. Rev. Lett. **88**, 047401 (2002).
[14] W. Langbein, in *Proc. 26th Int. Conf. on the Physics of Semiconductors* (2002).
[15] W. Langbein, J. Phys.: Condens. Matter **16**, S3645 (2004).
[16] W. Langbein, Rivista del nuovo cimento **33**, 255 (2010).
[17] M. Herman and H. Sitter, *Molecular Beam Epitaxy* (Springer-Verlag Berlin, 1989).
[18] H. Kawada, S. Shirayone, and K. Takahashi, Journal of Crystal Growth **128**, 550 (1993).
[19] U. Oesterle, R. P. Stanley, and R. Houdré, physica status solidi (b) **242**, 2157 (2005), ISSN 1521-3951, URL `http://dx.doi.org/10.1002/pssb.200560971`.
[20] A. M. Andrews, J. S. Specka, A. E. Romanov, M. Bobeth, and W. Pompe, J. Appl. Phys. **91**, 1933 (2002).
[21] S. Adachi, *Properties of Aluminium Gallium Arsenide* (INSPEC, London, 1988).
[22] J. W. Matthews and A. E. Blakeslee, J. Crystal Growth **27**, 118 (1974).
[23] M. Ettenberg and R. Paff, Journal of Applied Physics **41**, 3926 (1970).
[24] M. Shinohara, T. Ito, and Y. Imamura, J. Appl. Phys **58**, 3449 (1985).
[25] J. G. Grabmaier and C. B. Watson, physica status solidi (b) **32**, K13 (1969).
[26] K. Bacher and J. J. S. Harris, J. Electrochem. Soc. **142**, 2386 (1995).
[27] L. A. Giannuzzi and F. A. Stevie, eds., *Introduction to focused ion beams: instrumentation, theory, techniques, and practise* (Springer-Verlag Berlin, 2005).